DOI: 10.19884/j.1672-5220.202502010

Interconnected Ion Transport Channels Enabled by Enhanced Microphase-Separated Anion-Conductive Polymers for Anion Exchange Membrane Fuel Cells

YU Zhenguo, JIN Junhong, YANG Shenglin, LI Guang, ZHANG Jingjing*
State Key Laboratory of Advanced Fiber Materials, College of Materials Science and Engineering, Donghua University, Shanghai 201620, China

Abstract: The performance of anion exchange membrane fuel cells (AEMFCs) is severely constrained by the low OH^- conductivity of anion-conductive polymers. Although increasing the ion exchange capacity of these polymers through microstructural design effectively improves the OH^- conductivity, it often compromises the mechanical strength. To address this issue, we report enhanced microphase-separated structures in poly (styrene-*b*-(ethylene-*co*-butylene)-*b*-styrene) (SEBS)-based anion-conductive polymers, achieved through the synergy of hydrophilic quaternary ammonium (QA) groups and hydrophobic fluorinated side chains. Specifically, by precisely tuning the fluorine grafting degree of the polymer side chains, highly interconnected nanoscale ion-conducting domains are created, forming a three-dimensional (3D) pathway for efficient ion transport in anion exchange membranes (AEMs). Additionally, the mechanical stability of AEMs is strengthened by minimizing swelling. As a result, the QA- and fluorine-grafted AEM with a molar proportion of 4-fluorophenethylamine-modified blocks to styrene blocks of 30% (denoted as QSEBS-FPh_{30}) achieves a high OH^- conductivity of 100.86 mS/cm at 80 ℃ and a moderate tensile strength of 19.89 MPa in a fully hydrated state. The AEMFC utilizing QSEBS-FPh_{30} exhibits a peak power density of 204.31 mW/cm^2 at a current density of 737.29 mA/cm^2 and 80 ℃, which is 1.4 times that of QA-grafted SEBS (QSEBS). These findings underscore the significant role of microphase separation coupled with maximized ionic domain connectivity in enhancing the OH^- conductivity of anion-conductive polymers, offering valuable insights for the rational design of high-performance AEMs.

Keywords: fuel cell; anion exchange membrane (AEM); microphase separation; interconnected ionic domain
CLC number: TQ342+.94 **Document code**: A
Article ID: 1672-5220(2026)02-0021-11

Open Science Identity (OSID)

0 Introduction

The development of renewable and eco-friendly energy sources has been rapidly accelerating to meet growing global energy demands and mitigate environmental damage[1-2]. Among these, anion exchange membrane fuel cells (AEMFCs) stand out as advanced and eco-friendly energy devices due to their cost-effectiveness (enabled by the use of non-precious metal catalysts) and high performance (enhanced oxygen reduction kinetics)[3-4]. Anion-conductive polymers, which serve as anion exchange membranes (AEMs) and anion exchange ionomers (AEIs), play a critical role in facilitating efficient anion conduction[5]. However, significant challenges remain for anion-conductive polymers, particularly in addressing their low OH^- conductivity and insufficient alkaline stability, which continue to hinder the commercialization of AEMFCs[6].

A straightforward strategy to improve the OH^- conductivity of anion-conductive polymers is to increase their ion exchange capacity (IEC)[7]. However, increasing the IEC often results in excessive water uptake (WU)[8], which weakens intermolecular interactions within the polymer chains. This can lead to polymer swelling, ultimately compromising the mechanical properties[9-10]. Additionally, excessive swelling in AEIs can disrupt gas diffusion and electron conduction within the catalyst layers[11-12]. As a result, alternative strategies that enhance OH^- conductivity without significantly increasing the IEC are essential for developing high-performance anion-conductive polymers. One promising way is the design of phase-separated structures between hydrophilic and hydrophobic microdomains in block copolymers[13-14], where one polymer block can incorporate ion-conducting moieties, while the other remains nonionic. The natural tendency of the nonionic polymer blocks and cationic groups to aggregate separately leads to the formation of hydrophobic/hydrophilic microphase-separated structures. These structures provide a balance between OH^- conductivity and mechanical strength[15].

In addition to improving OH^- conductivity, enhancing the stability of anion-conductive polymers under high-temperature and alkaline conditions remains a significant challenge[16]. The chemical stability of these polymers is influenced by the composition of their

Received date: 2025-02-21
* Correspondence should be addressed to ZHANG Jingjing, email: jjzhang1@dhu.edu.cn
Citation: YU Z G, JIN J H, YANG S L, et al. Interconnected ion transport channels enabled by enhanced microphase-separated anion-conductive polymers for anion exchange membrane fuel cells[J]. *Journal of Donghua University (English Edition)*, 2026, 43(2): 21-31.

polymer backbones, ion-conducting head groups, and grafting strategies. Aromatic polymers, such as poly(phenyleneoxide)[17], poly(sulfone)[18], and poly(aryl ether ketone)[19], are commonly used polymer backbones. However, their aryl-heteroatom segments are prone to attack by OH^-. This degradation of the polymer backbone reduces both the chemical and mechanical stability of the material[20-21]. In contrast, aliphatic poly(styrene-*b*-(ethylene-*co*-butylene)-*b*-styrene) (SEBS) block copolymers, which lack heteroatoms, demonstrate greater potential for enhancing the alkaline resistance of anion-conductive polymers[22]. SEBS also exhibits a distinct microphase-separated structure, where the rigid polystyrene phase is well-separated from the flexible poly(ethylene-*co*-butylene) phase[23]. Strategies such as increasing the number of cations have been employed to further optimize phase separation of SEBS to improve its OH^- conductivity[24-25]. However, these strategies lead to the formation of large but isolated ion clusters, which may reduce OH^- conductivity and result in excessive WU and swelling[26-29]. Therefore, systematic investigations linking the ionic domain connectivity in SEBS to its ion conduction and mechanical properties are highly desired.

In this study, we began with the perspective of "structure-performance", proposed a cooperative strategy involving hydrophilic quaternary ammonium (QA) groups and hydrophobic fluorinated side chains to construct enhanced microphase-separated SEBS. By systematically tuning the grafting degree of two distinct types of side chains, we investigated their effects on the micro-morphology, mechanical properties, and OH^- conductivity of AEMs. Additionally, the practical applicability of AEMs was assessed via single fuel cell testing.

1 Materials and Methods

1.1 Materials

SEBS (Kraton™ A1535) was obtained from Kraton Performance Polymers Trading (Shanghai), Co., Ltd., China. Trichloromethane, *p*-xylene, anhydrous ethanol, tetrahydrofuran, and isopropanol were purchased from Sinopharm Co., Ltd., China. 1,4-Bis(chloromethoxy) butane (BCMB) was acquired from Xi'an Langene Biotechnology Co., Ltd., China. Anhydrous tin tetrachloride ($SnCl_4$) was purchased from Shanghai Aladdin Biochemical Technology Co., Ltd., China. Aqueous trimethylamine and 4-fluorophenethylamine were obtained from Shanghai Macklin Biochemical Co., Ltd., China. A platinum-carbon (Pt/C) catalyst (Pt mass fraction of 60%) was obtained from Suzhou Sinero Technology Co., Ltd., China. The gas diffusion layer (GDL) 28BC was acquired from SGL Carbon SE, Germany.

1.2 Methods

1.2.1 Preparation of chloromethylated SEBS (CMSEBS) polymer

Firstly, 3 g SEBS was dissolved in 90.0 mL trichloromethane in a three-necked flask for chloromethylation. After the reaction, 2.1 mL $SnCl_4$ was added to the solution, and the mixture was stirred continuously. The mixture was then placed in an ice-water bath for 30 min, after which 13.8 mL BCMB was added dropwise. The reaction was maintained at the same temperature for 10 h under N_2 atmosphere. Upon completion, the solution was poured into anhydrous ethanol to precipitate the polymer. After filtration, the polymer was dissolved in tetrahydrofuran and precipitated again in anhydrous ethanol for purification. The resulting white polymer was vacuum dried at 60 ℃ for 12 h to obtain CMSEBS.

1.2.2 Preparation of QA-grafted SEBS (QSEBS), and QA- and fluorine-grafted SEBS AEMs

The as-prepared CMSEBS was dissolved in trichloromethane and *p*-xylene to prepare a casting solution, which was poured onto a film casting machine to form a membrane. After drying at 40 ℃ in a vacuum oven for 12 h, the membrane was peeled off, cut into strips, and soaked in a 30% (mass fraction) trimethylamine aqueous solution for 48 h to obtain QSEBS, corresponding to 100% of the molar amount of chloromethyl sites. The membranes were then soaked in a 1 mol/L KOH solution for 48 h, followed by water washing to remove the remaining KOH, and vacuum dried to obtain QSEBS AEMs.

To preserve chloromethyl sites for grafting fluorinated side chains, CMSEBS samples were immersed in trimethylamine solutions (80%, 70%, and 60% equivalents of chloromethylation sites) to obtain partially QA-grafted CMSEBS (CM-QSEBS). The membranes were then dried and immersed in a saturated 4-fluorobenzylamine solution in *p*-xylene at 80 ℃ for 24 h for fluorination. Afterward, they were soaked in 1 mol/L KOH solution for 48 h to obtain the OH^- form, washed to remove the remaining KOH, and vacuum dried to obtain QA- and fluorine-grafted SEBS (denoted as QSEBS-FPh_n, where n represents the molar proportion of 4-fluorophenethylamine-modified blocks to styrene blocks, and $n = 20$, 30, 40, corresponding to the molar proportion of 20%, 30%, and 40%, respectively) AEMs.

1.3 Characterization

^1H nuclear magnetic resonance (NMR) spectra were obtained with an NMR spectrometer (AVANCE III HD 400 MHz, Bruker, Switzerland) by using deuterochloroform ($CDCl_3$) as a solvent and tetramethylsilane as an internal reference. Fourier transform infrared (FTIR) spectra were obtained with an FTIR spectrometer (Spectrum BXII, PerkinElmer,

USA). Thermogravimetric (TG) analysis was conducted by a TG spectrometer (TGA8000, PerkinElmer, USA) under N_2 atmosphere with an increase rate of 10 ℃/min from 50 to 800 ℃. Water contact angles (WCAs) were tested by a contact angle measuring instrument (OCA40Micro, Dataphysics, Germany). Scanning electron microscopy (SEM) images were acquired with a field-emission microscope (SU-8010, Hitachi, Japan). Atomic force microscopy (AFM) images were obtained with an atomic force microscope (Dimension FastScan, Bruker, USA). Small-angle X-ray scattering (SAXS) spectra were obtained with an SAXS spectrometer (Xeuss 2.0, Xenocs, France), and an enhanced two-dimensional (2D) position-sensitive proportional counter (PSPC) detector was used to record the scattering X-ray intensity. The inter-domain spacing d is the average distance between the phase domains in the AEMs, and it is calculated as

$$d = 2\pi/q, \tag{1}$$

where q is the magnitude of the scattering vector obtained from the test.

The membranes were soaked in water for 24 h before testing. Tensile strength and elongation of the wet membranes were measured by using a universal testing machine (Instron 1185, Instron, USA) at a test speed of 10 mm/min.

IEC was measured by using back titration. The membranes were soaked in a 0.010 mol/L HCl solution (50 mL) at room temperature for 24 h, and titrated with 0.005 mol/L KOH solution until the pH reached 7.

$$I = (c_1v_1 - c_2v_2)/m, \tag{2}$$

where I represents the IEC; c_1 and c_2 are the concentrations of the standard HCl solution and standard KOH solution, respectively; v_1 and v_2 are the volumes of the standard HCl solution and standard KOH solution, respectively; m is the dry mass of the membrane.

The swelling ratio (SR) and WU of the membranes were tested as follows. The masses and dimensions of the membranes were first measured, and then the samples were soaked in water at 25–80 ℃ for 24 h. After blotting the surface with filter paper, the wet masses and lengths were recorded.

$$K = [(L_1 - L_2)/L_2] \times 100\%, \tag{3}$$

$$W = [(m_1 - m_2)/m_2] \times 100\%, \tag{4}$$

where K represents the SR; W represents the WU; L_1 and m_1 are the length and mass of the wet membrane, respectively; L_2 and m_2 are the length and mass of the dry membrane, respectively.

The OH^- conductivity σ was measured by using the alternating current impedance method with an electrochemical workstation (Solartron 1470E, AMETEK, UK). Before test, the membranes were soaked in water for 24 h. The test temperature was varied from 25 to 80 ℃, and the alternating current (AC) frequency ranged from 1×10^6 to 1 Hz.

$$\sigma = t/(R_{AC}S), \tag{5}$$

where t is the thickness of the membrane; S is the area of the electrode; R_{AC} is the resistance determined by the AC impedance.

The activation energy E_a quantifies the energy barrier that ions must overcome to migrate through the polymer matrix. It is derived from the temperature dependence of OH^- conductivity by using the Arrhenius equation.

$$E_a = RT\ln\left(\frac{A}{\sigma}\right), \tag{6}$$

where R is the universal gas constant with a value of 8.314 J/(mol·K); T stands for the temperature; A is the pre-exponential factor related to the carrier concentration and attempt frequency.

The single-cell performance test followed a sequential workflow. It began with catalyst ink preparation, where 100 mg Pt/C was dispersed in water and isopropanol by adding the isopropanol in several increments, with ultrasonication performed after each addition, followed by the addition of an ionomer-trichloromethane solution and further mixing. This ink was then sprayed onto the membrane to achieve a Pt loading of 0.5 mg/cm^2 over an area of 2.5 cm × 2.5 cm, after which the membrane was activated in 1 mol/L KOH solution for 24 h and thoroughly rinsed. For assembly, the hydrated membrane was placed directly between two 28BC gas diffusion layers without hot pressing, sealed with 150 μm Teflon gaskets, and clamped by using eight bolts tightened to 6 N·m. Finally, the cell was tested at 80 ℃ with H_2/air reactants at 0.5 L/min, 100% relative humidity, and 0.1 MPa backpressure, undergoing activation at 0.75 V until the current density stabilized. It is important to note that these specific testing parameters are optimized for this setup and should be adjusted according to individual experimental conditions.

Electrochemical impedance spectroscopy (EIS) was conducted under in-situ conditions with a current density of 500 mA/cm^2, a frequency range of 1×10^4 to 0.1 Hz, and a 10% current signal perturbation amplitude.

2 Results and Discussion

2.1 Structural and morphological characterization

The preparation of QSEBS-FPh$_n$ involves three steps (Fig. 1(a)). Firstly, CMSEBS is generated by a chloromethylation reaction, where the chloromethyl groups are grafted onto the benzene ring of SEBS. The ^{1}H NMR spectra of CMSEBS and SEBS are shown in Fig. 1(b). The signal peak at a chemical shift of 4.5, corresponding to the hydrogen of the chloromethyl group, confirms successful chloromethylation. The signal peaks at chemical shift of 6.2–7.2 correspond to the hydrogen on the benzene ring of the polystyrene block. With 100% chloromethylation, the ratio of the two hydrogen signal

peaks is 1 ∶ 2. Integrating the hydrogen signal peaks at 4.5 and 6.2 – 7.2 verifies that the chloromethylation degree is 100%[30]. The emergence of stretching vibration absorption peaks, attributed to the C—Cl bond, is observed at 1 263 and 823 cm^{-1} for CMSEBS in comparison to SEBS in the FTIR spectra (Fig. 1(c)), further confirming the successful chloromethylation of CMSEBS. Secondly, all chloromethyl sites of CMSEBS are substituted with trimethylamine via the Menschutkin reaction to obtain QSEBS. The absorption peaks observed at 3 400 and 1 636 cm^{-1} are attributed to the stretching vibrations of O—H and C—N bonds, respectively (Fig. 1(c))[25, 31]. In the case of QSEBS-FPh$_n$, partial chloromethyl sites are replaced, while the remaining sites are utilized for the following fluorination modification. Finally, the residual chloromethyl sites are replaced with fluorine-grafted side chains by reacting with the amino group of 4-fluorophenethylamine through a Hofmann alkylation, which gives rise to new absorption peaks between 1 100 and 1 250 cm^{-1}, corresponding to the stretching vibration of aryl—F for QSEBS-FPh$_n$[29]. Additionally, the peak intensity increases as the proportion of fluorine-grafted side chains increases.

The morphology of the AEM significantly influences its properties. An uneven surface can adversely affect battery assembly and compromise the mechanical integrity of the AEM. For instance, QSEBS-FPh$_{30}$ exhibits a flat and smooth surface (Fig. 1(d)), devoid of prominent protrusions or ruptures. The cross-sectional thickness measures 30 μm (Fig. 1(e)), and the internal structure is characterized by a dense and uniform composition, free from impurities. This observation indicates that the AEM has remained intact throughout the preparation process. Furthermore, as evidenced by the optical photograph of QSEBS-FPh$_{30}$ (Fig. 1(f)), the excellent membrane-forming property of SEBS facilitates the large-area fabrication of the AEM, making it highly suitable for fuel cell applications.

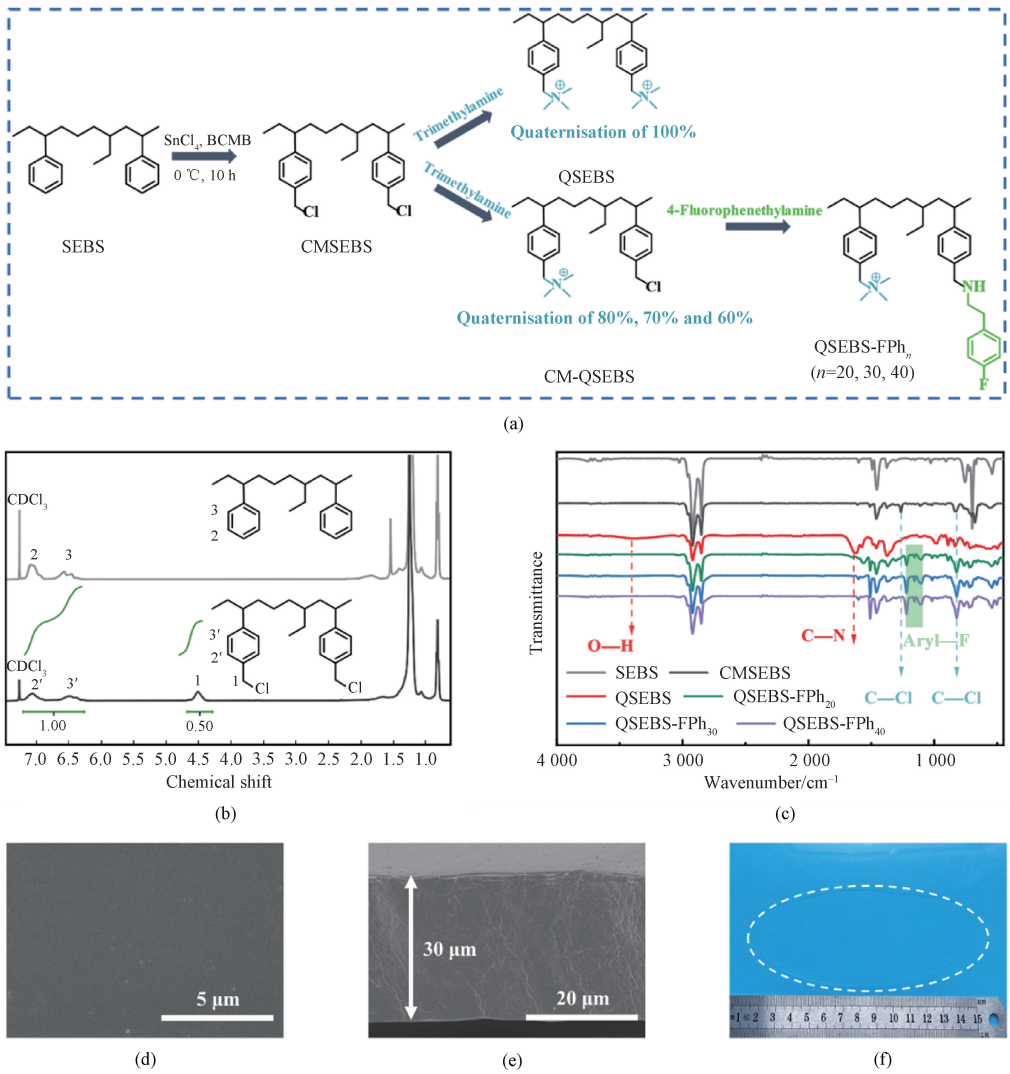

Fig. 1 Structural and morphological characterization: (a) synthesis pathways of QSEBS-FPh$_n$; (b) ^{1}H NMR spectra of CMSEBS and SEBS; (c) FTIR spectra of SEBS, CMSEBS, QSEBS, and QSEBS-FPh$_n$; (d) surface SEM image of QSEBS-FPh$_{30}$; (e) cross-sectional SEM image of QSEBS-FPh$_{30}$; (f) optical photograph of QSEBS-FPh$_{30}$

2.2 Physical properties

IEC is defined as the number of millimoles of cationic groups per gram of membrane. It directly determines the OH^- conductivity of the AEM. Additionally, the WU and SR are associated with the OH^- conductivity magnitude and the dimensional stability of the membrane. Generally, a higher IEC results in increased WU and SR of the membrane, which is crucial for evaluating the AEM performance. Consequently, it is essential to maintain the IEC in an appropriate range. Table 1 illustrates the WCA, IEC, WU, and SR of the AEMs.

Table 1 WCA, IEC, WU, and SR of QSEBS and QSEBS-FPh$_n$

AEM	WCA/(°)	IEC/(mmol/g)	WU/%				SR/%			
			25 ℃	40 ℃	60 ℃	80 ℃	25 ℃	40 ℃	60 ℃	80 ℃
QSEBS	52.6	2.28	27.8	57.6	80.0	105.6	11.4	15.6	16.8	29.3
QSEBS-FPh$_{20}$	76.3	1.89	10.1	15.9	16.8	18.1	2.0	3.9	7.2	11.5
QSEBS-FPh$_{30}$	99.6	1.60	8.8	11.1	14.4	16.2	1.9	2.6	4.1	7.0
QSEBS-FPh$_{40}$	107.4	1.32	2.7	4.5	6.3	12.7	1.8	2.4	3.0	4.6

It can be observed that the IEC and wettability of the AEMs decrease with the introduction of fluorinated side chains. This phenomenon occurs because the fluorinated side chains occupy the chloromethyl sites, thereby reducing the proportion of cationic groups available for modification. The decline in the proportion of hydrophilic groups, combined with the introduction of hydrophobic fluorinated side chains, results in a decrease in the wettability of the membrane and an increase in its hydrophobicity. The WU and SR values of QSEBS reach 27.8% and 11.4% at 25 ℃, respectively, which increase to 105.6% and 29.3% at 80 ℃ due to the enhanced movement of polymer chains with more free volume. In contrast, the grafting of fluorinated side chains in QSEBS-FPh$_n$ effectively mitigates the water absorption and swelling of membranes. The SR of QSEBS-FPh$_{40}$ is as low as 4.6% at 80 ℃, exhibiting minimal dimensional alteration. QSEBS-FPh$_{20}$ and QSEBS-FPh$_{30}$ also demonstrate good dimensional stability at 80 ℃, with the SR values of 11.5% and 7.0%, respectively. This stability enhances their mechanical properties and also facilitates the assembly and utilization of the membranes.

The mechanical and thermal properties of QSEBS and QSEBS-FPh$_n$ are shown in Fig. 2. The tensile strength of QSEBS in a fully hydrated state is 5.44 MPa, whereas QSEBS-FPh$_{30}$ exhibits a significant increase to 19.89 MPa (Fig. 2(a)), representing an improvement of approximately 266%.

Thermal stability of AEMs is crucial in determining the lifespan of AEMFCs. As demonstrated by the TG analysis (Fig. 2(b)), all the AEMs display a minor degradation peak at 100 ℃, which can be attributed to the volatilization of water[32]. For QSEBS, a significant degradation occurs near 200 ℃ with a mass loss fraction of 14.1% due to the degradation of the QA-grafted side chains. Additionally, the mass loss observed near 450 ℃ for all the AEMs is attributed to the degradation of the polymer backbone. From the results of the thermal stability tests, it can be concluded that QSEBS-FPh$_n$ can meet the temperature requirements of practical fuel cell applications.

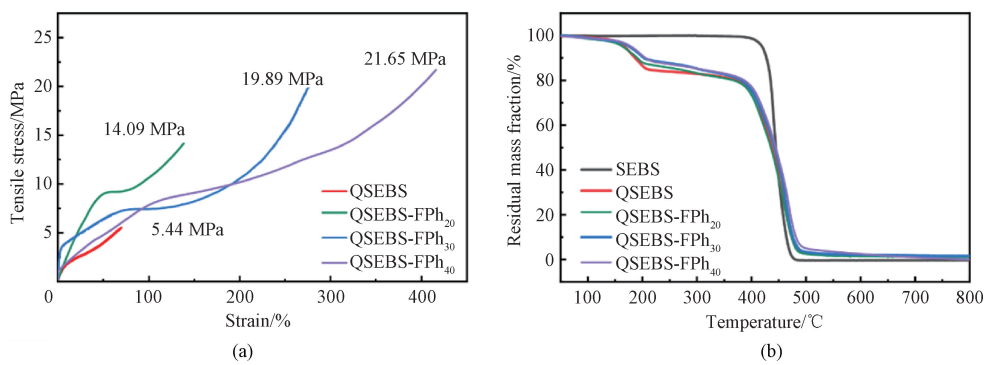

Fig. 2 Mechanical and thermal properties of QSEBS and QSEBS-FPh$_n$: (a) stress-strain curves; (b) TG curves

2.3 Micro-morphology and ionic conductivity

Membrane micro-morphology is a key performance factor, especially for the diffusion of OH^-. Highly connected ionic domains formed by hydrophilic and hydrophobic phase separation are crucial for ion migration. In the AFM images of AEMs (Fig. 3(a)), the dark regions represent a hydrophilic microphase containing QA functional groups, while the bright regions originate from the hydrophobic microphase comprising the fluorinated side chains. In QSEBS, ion clusters are agglomerated

and randomly distributed throughout the hydrophobic microphase. For comparison, the introduction of fluorinated side chains leads to a significant reduction in the size of the hydrophilic regions for QSEBS-FPh_{20} and QSEBS-FPh_{30}. When the modification degree of fluorinated side chains increases to 30%, well-defined hydrophilic domains with significantly improved connectivity are observed. We attribute this change in connectivity to the thermodynamic incompatibility between the hydrophilic QA ion clusters and the hydrophobic fluorinated side chains in the styrene block. However, when the fluorine atom content in QSEBS-FPh_{40} further increases, a significant number of fluorinated side chains act as spacers, disrupting the formation of interconnected ionic clusters. These results are further supported by the findings of the SAXS test (Fig. 3(b)). The q values of QSEBS, QSEBS-FPh_{20}, QSEBS-FPh_{30}, and QSEBS-FPh_{40} are 0.055 9, 0.091 5, 0.105 7, and 0.119 9 nm^{-1}, respectively, corresponding to the inter-domain spacings of 112.34, 68.63, 59.41, and 52.38 nm, respectively. The optimized immiscibility between hydrophilic cation structure and hydrophobic sidechain segments promotes microphase separation with the improvement of ion channel connectivity.

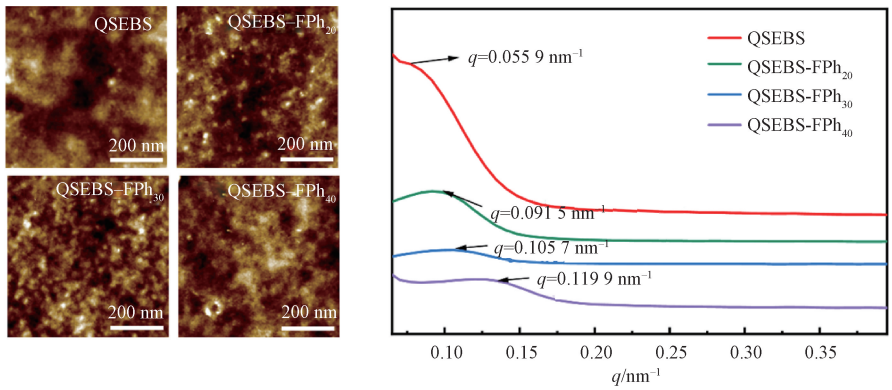

Fig. 3 Morphologies of QSEBS and QSEBS-FPh_n: (a) AFM images; (b) SAXS curves

Driven by the microphase separation and self-assembly of hydrophilic ion clusters and hydrophobic groups, the nanoscale continuous ion transport channels modify the pathways of ion transport, thereby further influencing the ion transport capacity of the membrane. To quantify the performance improvements resulting from this structural optimization, the OH^- conductivity of four types of AEMs was evaluated at temperatures ranging from 25 to 80 ℃. As presented in Fig. 4(a), QSEBS-FPh_n demonstrates a significant enhancement in OH^- conductivity compared to QSEBS. Notably, QSEBS-FPh_{30} exhibits the highest OH^- conductivity (100.86 mS/cm at 80 ℃), which is about 1.4 times that of QSEBS (72.46 mS/cm). This enhancement meets the requirements of AEMs in terms of OH^- conductivity (≥ 100 mS/cm at 80 ℃) and is primarily attributed to the interconnected ionic domains of the membrane[33-35]. Additionally, the activation energies of QSEBS and QSEBS-FPh_n are also calculated by the Arrhenius equation to further explain the improvement of OH^- conductivity (Fig. 4(b)). The lowest E_a (11.35 kJ/mol) indicates the highest OH^- conductivity for QSEBS-FPh_{30}, which is consistent with the conductivity distribution. The enhanced microphase separation, along with the well-connected ionic groups in the hydrophilic domain, establishes an interconnected high-speed OH^- transport channel throughout the membranes, greatly enhancing the ion transport property (Fig. 4(c)).

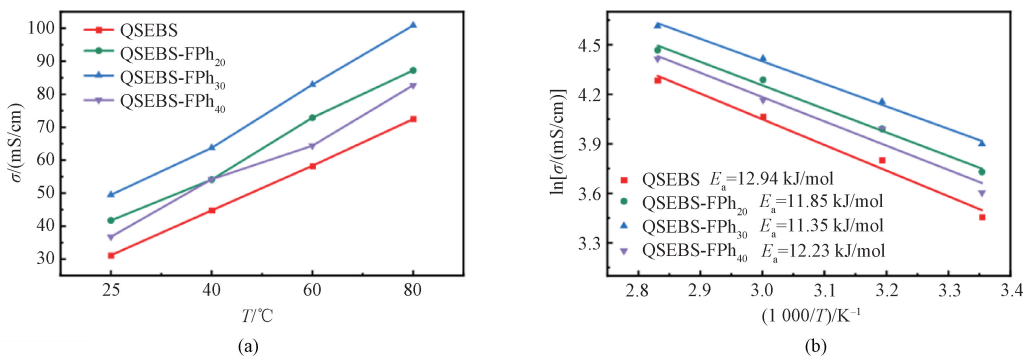

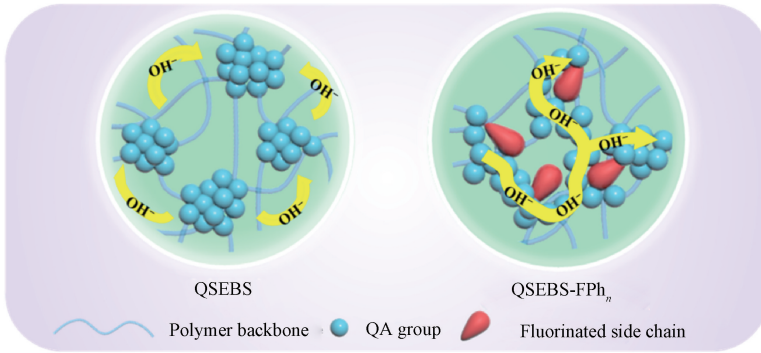

(c)

Fig. 4 Ion transport properties of QSEBS and QSEBS-FPh$_n$: (a) OH^- conductivity; (b) Arrhenius plots; (c) schematic illustration of ion transport mechanism

Comparison of QSEBS-FPh$_{30}$ with other SEBS-based AEMs in terms of SR, tensile strength, and OH^- conductivity is shown in Table 2. QSEBS-FPh$_{30}$, which features efficient interconnected ionic transport channels, achieves a moderately high OH^- conductivity of 100.86 mS/cm while maintaining excellent swelling control with an SR of 7.0% and a moderate tensile strength of 19.89 MPa. This highlights the benefits of the interconnected ionic transport channels derived from the enhanced microphase separation structure in improving the overall performance of AEMs.

Table 2 Comparison of QSEBS-FPh$_{30}$ with other SEBS-based AEMs

SEBS-based AEM	SR at 80 ℃ /%	Tensile strength/MPa	σ at 80 ℃/(mS/cm)	Ref.
QSEBS-FPh$_{30}$	7.0	19.89	100.86	This work
SEBS1401-OH	12.0	22.1	80.5	[36]
TDMAP-50X-SEBS	16.7	12.3	109.9	[37]
SEBS-P_2O_6	9.2	—	11.7	[38]
70C16-SEBS-TMHDA	9.3	18.03	72.13	[39]
Pi-POSS$_{15\%}$/Pi-SEBS	34.2	30.75	69.1	[31]
SEBSC6-Pip	42.0	51.6	57.7	[40]
SEBS-p-ASU-TMA-40	35	11.12	96.6	[41]
SEBS-C16-20C4	10.9	11.41	77.78	[42]

2.4 Electrochemical performance

The polarization and power density curves are presented in Fig. 5(a), where the left *y*-axis represents cell voltage and the right *y*-axis represents power density. QSEBS, QSEBS-FPh$_{20}$, QSEBS-FPh$_{30}$, and QSEBS-FPh$_{40}$ in Fig. 5 represent single cells assembled by using QSEBS and a series of QSEBS-FPh$_n$ AEMs. The open-circuit voltages of all the cells exceed 0.9 V, indicating that the obtained four AEMs effectively block gas crossover as reported in Ref. [43]. The highest peak power density (204.31 mW/cm^2) is achieved at a current density of 737.29 mA/cm^2 for the cells with QSEBS-FPh$_{30}$, representing a performance improvement of about 40% compared with the cells based on QSEBS with the same ionomer (145.91 mW/cm^2 at 537.47 mA/cm^2). Cells with QSEBS-FPh$_{20}$ and QSEBS-FPh$_{40}$ exhibit lower peak power density than those with QSEBS-FPh$_{30}$ due to the lower OH^- conductivity.

EIS measurements were performed to examine the relationship between AEM structures and fuel cell performance. The results are shown in Fig. 5(b), where Z' represents the real part of complex impedance, and Z'' denotes the imaginary part. The impedance spectra are simulated by using the equivalent circuit depicted in Fig. 5(c). R_i represents the total ohmic resistance, influenced by the intrinsic resistance of each component and interfacial contact resistance; $R_{a,ct}$ and $R_{c,ct}$ correspond to the charge transfer resistances at the anode and cathode, respectively; CPE_a and CPE_c represent the constant phase elements at the anode and cathode, respectively.

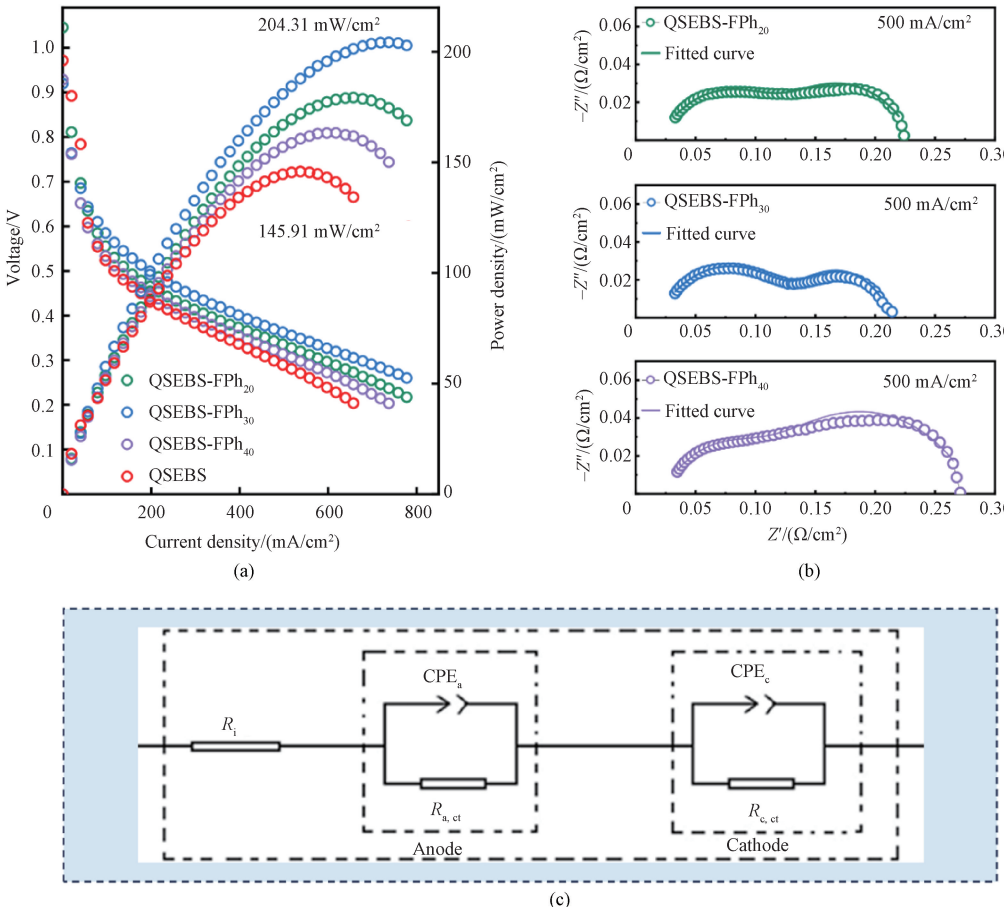

Fig. 5 Electrochemical performance of AEMFCs based on QSEBS and QSEBS-FPh$_n$: (a) single-cell performance; (b) EIS spectra; (c) equivalent circuit model for impedance analysis

The simulated resistances derived from the EIS test of AEMFCs based on QSEBS-FPh$_n$ are shown in Table 3.

Table 3 Simulated resistances derived from EIS test of AEMFCs based on QSEBS-FPh$_n$

AEMFC	Current density/(mA/cm^2)	R_i/(Ω/cm^2)	$R_{a,ct}$/(Ω/cm^2)	$R_{c,ct}$/(Ω/cm^2)
QSEBS-FPh$_{20}$	500	0.018	0.104	0.110
QSEBS-FPh$_{30}$	500	0.016	0.116	0.078
QSEBS-FPh$_{40}$	500	0.022	0.086	0.174

As shown in Table 3, AEMFCs with QESBE-FPh$_n$ show similar ohmic resistances (near 0.020 Ω/cm^2), with R_i much lower than $R_{a,ct}$ and $R_{c,ct}$. This indicates that all three cells have achieved sufficient hydration under the test conditions, and the charge transfer resistance at both electrodes is the main factor affecting the cell's performance. The cell based on QSEBS-FPh$_{30}$ exhibits the lowest cathodic charge transfer resistance at a current density of 500 mA/cm^2. The excellent hydroxide transport capacity of QSEBS-FPh$_{30}$ ensures efficient OH^- conductivity from the cathode to the anode, preventing localized accumulation on the catalyst surface. This exposes more catalyst sites for oxygen reduction, resulting in the lowest cathodic charge transfer resistance. Additionally, the high OH^- conductivity enhances water production at the anode, maintaining membrane hydration but potentially hindering the hydrogen reduction reaction in the anodic catalyst layer[44]. This results in a slightly higher anodic charge transfer impedance for QSEBS-FPh$_{30}$.

3 Conclusions

This study designs fluorinated SEBS-based AEMs with enhanced microphase-separated structures, incorporating QA groups as hydrophilic cations and fluorinated side chains as hydrophobic units. The impact of varying fluorine-grafted degrees on the AEMs' microstructure, physical properties, and electrochemical properties was systematically explored. The findings

emphasize the crucial role of ionic domain connectivity in achieving high OH^- conductivity. For QSEBS-FPh_{30}, the increase in incompatibility between its hydrophilic and hydrophobic segments reduces the ionic cluster size, resulting in well-connected nanosized ionic domains and enhanced OH^- conductivity. Additionally, the microphase-separated structure limits swelling, crucial for maintaining dimensional and mechanical stability. QSEBS-FPh_{30} shows excellent performance, with a high OH^- conductivity of 100.86 mS/cm at 80 ℃, a low SR of 7.0% at 80 ℃, and a moderate tensile strength of 19.89 MPa in a fully hydrated state. Consequently, the AEMFC with QSEBS-FPh_{30} achieves significantly improved electrochemical performance, with a peak power density of 204.31 mW/cm^2 at a current density of 737.29 mA/cm^2 and 80 ℃. This study offers a new strategy for designing anion-conductive polymers with controlled domain size and connectivity, showing great potential for next-generation AEMFC development.

References

[1] JANNASCH P, WEIBER E A. Configuring anion-exchange membranes for high conductivity and alkaline stability by using cationic polymers with tailored side chains[J]. *Macromolecular Chemistry and Physics*, 2016, 217(10): 1108-1118.

[2] VARCOE J R, ATANASSOV P, DEKEL D R, et al. Anion-exchange membranes in electrochemical energy systems[J]. *Energy & Environmental Science*, 2014, 7(10): 3135-3191.

[3] KIM S, HER M, KIM Y, et al. The impact of the catalyst layer structure on the performance of anion exchange membrane fuel cell[J]. *Electrochimica Acta*, 2021, 400: 139439.

[4] MUSTAIN W E, MUSTAIN W, CHATENET M, et al. Durability challenges of anion exchange membrane fuel cells[J]. *Energy & Environmental Science*, 2020, 13(9): 2805-2838.

[5] CHEN N J, LEE Y M. Anion exchange polyelectrolytes for membranes and ionomers[J]. *Progress in Polymer Science*, 2021, 113: 101345.

[6] ZHANG J J, ZHANG K Y, LIANG X, et al. Self-aggregating cationic-chains enable alkaline stable ion-conducting channels for anion-exchange membrane fuel cells[J]. *Journal of Materials Chemistry A*, 2021, 9(1): 327-337.

[7] LIN B C, XU F, SU Y, et al. Ether-free polybenzimidazole bearing pendant imidazolium groups for alkaline anion exchange membrane fuel cells application[J]. *ACS Applied Energy Materials*, 2020, 3(1): 1089-1098.

[8] HAN J J, ZHU L, PAN J, et al. Elastic long-chain multication cross-linked anion exchange membranes[J]. *Macromolecules*, 2017, 50(8): 3323-3332.

[9] GU S, CAI R, YAN Y S. Self-crosslinking for dimensionally stable and solvent-resistant quaternary phosphonium based hydroxide exchange membranes[J]. *Chemical Communications*, 2011, 47(10): 2856-2858.

[10] PAN J, LU S F, LI Y, et al. High-performance alkaline polymer electrolyte for fuel cell applications[J]. *Advanced Functional Materials*, 2010, 20(2): 312-319.

[11] SAIDIN N U, JEHAN O S, LEONG K S, et al. Influence of ionomer concentration and membrane thickness on membrane electrode assembly in alkaline fuel cell performance[J]. *Asia-Pacific Journal of Chemical Engineering*, 2024, 19(2): e3024.

[12] EON C J, CHOI J, LEE S, et al. Effects of fabrication parameters of membrane-electrode assembly for high-performance anion exchange membrane fuel cells[J]. *Journal of Industrial and Engineering Chemistry*, 2024, 133: 255-262.

[13] XIE N, WANG T, KANG H W, et al. Decisive effect of hydrophobic rigid-flexible coupled side chains of polycarbazoles on the performance of anion exchange membranes for fuel cells[J]. *ACS Applied Energy Materials*, 2024, 7(20): 9512-9524.

[14] LAI A N, WANG Z, LIN R K, et al. Tandem one-pot synthesis of block copolymers for anion exchange membranes[J]. *Journal of Applied Polymer Science*, 2024, 141(39): e55997.

[15] SHEN S Y, HAN A D, YAN X H, et al. Influence of equivalent weight of ionomer on proton conduction behavior in fuel cell catalyst layers[J]. *Journal of the Electrochemical Society*, 2019, 166(12): F724-F728.

[16] OHASHI H, JUNG H, CHI X Q, et al. Alkali-resistant anion exchange membranes with grafted polyelectrolyte for fuel cells[J]. *Chemistry Letters*, 2018, 47(7): 857-859.

[17] HOSSAIN M M, HOU J Q, WU L, et al. Anion exchange membranes with clusters of alkyl ammonium group for mitigating water swelling but not ionic conductivity[J]. *Journal of Membrane Science*, 2018, 550: 101-109.

[18] YAN J L, HICKNER M A. Anion exchange membranes by bromination of benzylmethyl-containing poly(sulfone)s[J]. *Macromolecules*, 2010, 43(5): 2349-2356.

[19] AHN Y, KIM D. Anion exchange membrane prepared from imidazolium grafted poly(arylene ether ketone) with enhanced durability for vanadium redox flow battery[J]. *Journal of Industrial and Engineering Chemistry*, 2019, 71: 361-368.

[20] YIN Z Y, WU Y Z, SHI B B, et al. Alkaline stable piperidinium-based biphenyl polymer for anion exchange membranes [J]. *Solid State Ionics*, 2022, 383: 115969.
[21] LEE W H, KIM Y S, BAE C. Robust hydroxide ion conducting poly(biphenyl alkylene)s for alkaline fuel cell membranes [J]. *ACS Macro Letters*, 2015, 4(8): 814-818.
[22] WANG F, CUI Y, SANG J, et al. Cross-linked of poly(biphenyl pyridine) and poly(styrene-*b*-(ethylene-*co*-butylene)-*b*-styrene) grafted with double cations for anion exchange membrane[J]. *Electrochimica Acta*, 2022, 405: 139770.
[23] JEON J Y, PARK S, HAN J, et al. Synthesis of aromatic anion exchange membranes by Friedel-Crafts bromoalkylation and cross-linking of polystyrene block copolymers [J]. *Macromolecules*, 2019, 52(5): 2139-2147.
[24] AL MUNSUR A Z, HOSSAIN I, NAM S Y, et al. Quaternary ammonium-functionalized hexyl bis(quaternary ammonium)-mediated partially crosslinked SEBSs as highly conductive and stable anion exchange membranes [J]. *International Journal of Hydrogen Energy*, 2020, 45(31): 15658-15671.
[25] GAO X Q, YU H M, QIN B W, et al. Enhanced water transport in AEMs based on poly(styrene-ethylene-butylene-styrene) triblock copolymer for high fuel cell performance [J]. *Polymer Chemistry*, 2019, 10(15): 1894-1903.
[26] HE Y B, SI J J, WU L, et al. Dual-cation comb-shaped anion exchange membranes: structure, morphology and properties [J]. *Journal of Membrane Science*, 2016, 515: 189-195.
[27] LONG C, ZHAO T, TIAN L, et al. Highly stable and conductive multicationic poly(biphenyl indole) with extender side chains for anion exchange membrane fuel cells[J]. *ACS Applied Energy Materials*, 2021, 4(6): 6154-6165.
[28] DANG H S, JANNASCH P. Exploring different cationic alkyl side chain designs for enhanced alkaline stability and hydroxide ion conductivity of anion-exchange membranes [J]. *Macromolecules*, 2015, 48(16): 5742-5751.
[29] AL MUNSUR A Z, LEE J, CHAE J E, et al. Hexyl quaternary ammonium- and fluorobenzoyl-grafted SEBS as hydrophilic-hydrophobic comb-type anion exchange membranes[J]. *Journal of Membrane Science*, 2022, 643: 120029.
[30] HAN J J, LIU C F, DENG C W, et al. Mechanically robust and highly conductive semi-interpenetrating network anion exchange membranes for fuel cell applications[J]. *Journal of Power Sources*, 2022, 548: 232097.
[31] SANG J, WANG Z, ZHU H. Functionalized POSS-modified SEBS-based composite anion-exchange membranes for AEMFCs[J]. *Energy & Fuels*, 2022, 36(20): 12780-12790.
[32] CHOI J, MIN K, MO Y H, et al. Understanding the effect of triazole on crosslinked PPO-SEBS-based anion exchange membranes for water electrolysis[J]. *Polymers*, 2023, 15(7): 1736.
[33] HU C, DENG X L, DONG X C, et al. Rigid crosslinkers towards constructing highly-efficient ion transport channels in anion exchange membranes[J]. *Journal of Membrane Science*, 2021, 619: 118806.
[34] DAS G, CHOI J H, NGUYEN P K T, et al. Anion exchange membranes for fuel cell application: a review[J]. *Polymers*, 2022, 14(6): 1197.
[35] HUA D X, HUANG J Z, FABBRI E, et al. Development of anion exchange membrane water electrolysis and the associated challenges: a review[J]. *ChemElectroChem*, 2023, 10(1): e202200999.
[36] SHI Y, ZHAO Z F, LIU W, et al. Physically self-cross-linked SEBS anion exchange membranes[J]. *Energy & Fuels*, 2020, 34(12): 16746-16755.
[37] LEE J, MIN K, JEON S, et al. Development of crosslinked SEBS-based anion exchange membranes for water electrolysis: investigation of the crosslinker effect[J]. *International Journal of Hydrogen Energy*, 2023, 48(63): 24180-24195.
[38] XU Z Q, WILKE V, CHMIELARZ J J, et al. Novel piperidinium-functionalized crosslinked anion exchange membrane with flexible spacers for water electrolysis[J]. *Journal of Membrane Science*, 2023, 670: 121302.
[39] WANG F H, LI C H, SANG J, et al. Synthesis and characterization of a long side-chain double-cation crosslinked anion-exchange membrane based on poly(styrene-*b*-(ethylene-*co*-butylene)-*b*-styrene) [J]. *International Journal of Hydrogen Energy*, 2021, 46(73): 36301-36313.
[40] YU N, DONG J H, LI H H, et al. Improving the performance of quaternized SEBS based anion exchange membranes by adjusting the functional group and side chain structure[J]. *European Polymer Journal*, 2021, 154: 110528.
[41] SANG J, YANG L C, WANG F H, et al. SEBS-based anion exchange membrane grafted with *N*-spirocyclic quaternary ammonium cations for fuel cells[J]. *ACS Applied Energy Materials*, 2022, 5(10): 12347-12358.
[42] LI Z M, LI C H, LONG C, et al. Elastic and durable multi-cation-crosslinked anion exchange membrane based on poly(styrene-*b*-(ethylene-*co*-butylene)-*b*-styrene) [J]. *Journal of Polymer Science*, 2020, 58(16): 2181-2196.
[43] LONG C, LU C R, LI Y X, et al. *N*-spirocyclic ammonium-functionalized graphene oxide-based

anion exchange membrane for fuel cells [J]. *International Journal of Hydrogen Energy*, 2020, 45(38): 19778-19790.
[44] ZHOU J, GUO J S, CHU D, et al. Impacts of anion-exchange-membranes with various ionic exchange capacities on the performance of H_2/O_2 fuel cells[J]. *Journal of Power Sources*, 2012, 219: 272-279.

应用于阴离子交换膜燃料电池的阴离子导电聚合物：通过增强微相分离结构实现互联离子传输通道

于振国，金俊弘，杨胜林，李　光，张晶晶*
东华大学 先进纤维材料全国重点实验室，材料科学与工程学院，上海 201620

摘　要：阴离子交换膜燃料电池(anion exchange membrane fuel cell，AEMFC)的性能受限于阴离子导电聚合物的低 OH^- 电导率。尽管通过微观结构设计提高这些聚合物的离子交换容量能够有效改善 OH^- 电导率，但往往会牺牲其力学强度。为解决这一问题，本文报道了一种基于聚(苯乙烯-*b*-(乙烯-*co*-丁烯)-*b*-苯乙烯)(poly(styrene-*b*-(ethylene-*co*-butylene)-*b*-styrene)，SEBS)的阴离子导电聚合物，通过亲水性季铵(quaternary ammonium，QA)基团与疏水性氟化侧链的协同作用，实现了增强的微相分离结构。通过精确调节聚合物侧链的氟接枝程度，可形成高度互联的纳米级离子导电域，从而在阴离子交换膜(anion exchange membrane，AEM)中构建了高效的三维离子传输通道。此外，通过减少溶胀，进一步增强了 AEM 的力学稳定性。当 4-氟苯乙胺改性链段与苯乙烯链段摩尔比为 30%时，所制备的 QA 和氟基双接枝改性的 AEM (QSEBS-FPh_{30})在 80 ℃下具有高 OH^- 电导率(100.86 mS/cm)，其在完全水合状态下具有良好的拉伸强度(19.89 MPa)。以 QSEBS-FPh_{30} 为电解质的 AEMFC 在 737.29 mA/cm^2 电流密度和 80 ℃下，达到 204.31 mW/cm^2 的峰值功率密度，是 QA 接枝 SEBS (QSEBS) 的 1.4 倍。研究结果表明了微相分离与最大化离子域连接性在提升阴离子导电聚合物 OH^- 电导率中的重要作用，为高性能 AEM 的合理设计提供了理论依据。

关键词：燃料电池；阴离子交换膜；微相分离；互联离子域